Research article

Effect of ball milling time on $Sr_{0.7}Sm_{0.3}Fe_{0.4}Co_{0.6}O_{2.65}$ perovskites and their application as semiconductor layers in dye-sensitized solar cells

Samantha Ndlovu [a], Edigar Muchuweni [a], Vincent O. Nyamori [a,*]

[a] School of Chemistry and Physics, University of KwaZulu-Natal, Westville Campus, Private Bag X54001, Durban 4000, South Africa

A R T I C L E I N F O

A B S T R A C T

The practical utilization of TiO_2 as a semiconductor in dye-sensitized solar cells (DSSCs) has been set back by poor visible light absorption, high charge carrier recombination, and low electrical conductivity, which reduce the power conversion efficiency (PCE) and sustainability of the device. In this respect, perovskites with excellent properties, such as large surface area, good optical properties, high electrical conductivity, and superior electrochemical stability, have recently emerged as promising alternatives capable of overcoming the drawbacks of TiO_2. Herein, $Sr_{0.7}Sm_{0.3}Fe_{0.4}Co_{0.6}O_{2.65}$ (SSFC) perovskites were prepared via the ball milling method at various milling times of 0, 5, and 10 h, and the obtained samples were denoted by SSFC-0, SSCF-5, and SSCF-10, respectively. Increasing the ball milling time led to a significant reduction in nanoparticle size and agglomeration, which, in turn, increased the surface area and electrical conductivity of the samples. As a consequence, the SSFC-10 perovskite exhibited the smallest average particle sizes (18.9 nm) with the largest surface area (61.8 $m^2 \, g^{-1}$) and minimum defects, which allowed for efficient electron transport, resulting in the best electrical conductivity of 49.8 S cm^{-1}. Ultimately, DSSCs fabricated using SSFC-10 semiconductor layers achieved an optimum PCE of 6.01 %, which is an improvement of 8.67 %, 1.1 %, and 6.56 % for SSFC-0 (3.69 %), SSFC-5 (4.96 %), and TiO_2 (5.64 %), respectively. Thus, varying the ball milling time can be used as an effective technique to tailor the physicochemical properties of SSFC to suit desired applications, particularly the fabrication of highly efficient and sustainable DSSC semiconductor layers.

1. Introduction

Dye-sensitized solar cells (DSSCs) are emerging third-generation photovoltaic devices that have recently drawn the attention of many researchers due to their low cost, environment-friendliness, facile fabrication procedures, and promising power conversion efficiency (PCE) under indoor and outdoor light [1,2]. Although laboratory-scale DSSCs have so far exhibited a PCE of more than 16 % [3,4], this PCE is still lower than that of commercially available silicon solar cells. In indoor photovoltaics (PVs), DSSCs have a promising PCE of more than 34 % and long-term device stability at ambient temperature [4]. Ricoh (a Japanese electronics company) has launched an indoor PV solid-state DSSC for integration with autonomous electronic devices and wireless sensors that use low electricity to power these devices [5]. Inspired by this, ongoing research aims to improve the performance and sustainability of DSSCs

further to compete with those of their silicon-based counterparts, thereby opening up the avenues for commercialization. If done, this is also envisaged to broaden the potential applications of DSSCs, especially in powering electronic devices under indoor or outdoor conditions.

A typical DSSC comprises three main components, namely, the photoanode, which is made up of a dye-coated semiconducting oxide film on a transparent conducting electrode [6], an electrolyte [7], and a counter electrode [8]. When light illuminates a DSSC, it passes through the transparent conducting oxide before being absorbed by the dye for exciton generation to occur. Ruthenium-based dyes [9] and natural dyes [10] have shown outstanding performance in recent years due to their broad absorption spectra, including the potential use of bio-based DSSCs [11]. The photoexcited electrons from the dye flow to the transparent conducting electrode through the semiconducting oxide for onward transfer to the external circuit before being collected at the counter electrode [12]. The counter electrode facilitates the rapid transfer of electrons from the external circuit to the electrolyte to catalyse the reduction of I_3^- to I^- for dye regeneration [13]. Pt has been commonly used as a counter electrode in DSSCs due to its high electrical conductivity and excellent electrocatalytic activity [14]. However, Pt is a costly noble metal; hence, there is need of replacing it with low-cost alternatives, such as Al [15] or the introduction of iron phosphide catalyst as a counter electrode in DSSCs [16].

Among the DSSC components, the photoanode is considered one of the main device components where the needed photoabsorption process occurs. In many cases, the photoanode is commonly made up of semiconductor metal oxide, usually TiO_2, which has a wide bandgap but is favourable due to its high photochemical stability, non-toxicity, abundance and low cost [17,18]. However, TiO_2 has a large band gap of ~3.2 eV, which allows for the absorption of ultraviolet (UV) light only, resulting in poor absorption of visible light, which, in turn, compromises electron-hole pair generation, thereby reducing the device performance [11,19]. In addition, the presence of many grain boundaries and defects in porous TiO_2 films restrict the efficient flow of photogenerated electrons from the dye to the transparent conducting electrode, which causes high charge carrier recombination. Also, the TiO_2 mesoporous structure allows the electrolyte to penetrate and reach the transparent conducting electrode, which causes the recombination of electrons on the transparent conducting electrode and holes in the electrolyte, resulting in short electron lifetimes [20,21]. There has been a drive to obtain suitable alternative anode semiconductors, including metal titania combined or doped with other metals such as Ag–Au@TiO_2 [22] and Ni-doped TiO_2 [23].

Therefore, for the anode component of the DSSCs, finding alternative suitable semiconductors with improved properties would open up new possibilities for enhancing the performance of the device. In this respect, perovskites have been recently applied as DSSC semiconductors with promising efficiency due to high electrical conductivity [24], resistance to photobleaching [24], and better stability in acidic dye [1]. For example, Sheikh et al. [24] prepared A_2LuTaO_6 (A = Ba, Sr, Ca) and used it as a highly conductive semiconductor layer in DSSCs with a PCE of 0.45 % (when A = Sr) compared to A = Ba (0.32 %) and A = Ca (0.28 %). In a similar study, Roy et al. [25] replaced TiO_2 with the $BnSnO_3$ perovskite and obtained DSSCs with a power conversion efficiency (PCE) of up to 6.86 %.

Perovskite oxides are generally formed from mixed oxides with the formula ABO_3, where the A and B-site cations can be partially substituted by rare and transition metal ions, respectively [26]. The strong bonding that takes place between the B-site cation and oxygen determines the crucial character of perovskite oxides [27]. Also, the A-site cation contributes to thermal resistance, while the B-site is responsible for catalytic activities [28–30]. Moreover, the introduction of cations, such as Sr and Fe, to $A_xA_{1-x}B_xB_{1-x}O_3$ can form a novel structure with good optical properties, low charge carrier recombination, excellent electrical conductivity, superior catalytic activity and high stability [31–33]. Lately, many mixed conducting oxides, such as $Pr_{0.6}Sr_{0.4}Fe_{0.8}Co_{0.2}O_3$ [34], $Ce_{0.6}Sr_{0.4}Fe_{0.8}Co_{0.2}O_3$ [35], $La_{1-x}Sr_xCo_{1-y}Fe_yO_3$ [36] and $Sr_xSm_{1-x}Fe_yC_{y-1}O_3$ [37], have been explored. Among them, $Sr_xSm_{1-x}Fe_yC_{y-1}O_3$ has received tremendous attention because the partial substitution of the bivalent cation Sr^{2+} can contribute to a low oxidation state, while the trivalent cation Sm^{3+} on the A-site can act as an electron acceptor to form oxygen vacancies [29]. This could further allow the formation of B-site cations in a high valence state. The strong interaction of A and B-site cations can increase the surface area and enhance the structural stability, subsequently improving conductivity, catalytic activity and sustainability [29,38].

Perovskites can be prepared using various methods, such as sol-gel [39], sonochemical [40], combustion [41], hydrothermal [42], co-precipitation [43], and ball milling [44]. Among them, ball milling is more efficient in improving particle size and morphology [45]. Ball milling is an advanced technique used to synthesize various functional materials with improved structure, shape, and crystallinity [46]. It uses mechanical energy from the constant collisions between milling balls and powder particles. Mechanical energy is created during milling at room temperature, promoting the phase reaction between compounds [45]. This method can function at a low reaction temperature and provide high-yield final products. The ball milling process can be influenced by many parameters, such as rotation speed, milling method, ball-to-powder ratio, and milling time [46]. Among these, milling time is considered the vital parameter of action for improving the physicochemical properties of perovskites. In recent years, significant developments have been made in ball milling by combining it with post-synthesis calcination at a moderate temperature level to avoid obtaining smaller surface areas and less stable catalysts [46–48].

Although many studies have reported the preparation of perovskites using repeated ball milling and calcining [49–53], to the best of our knowledge, there are limited studies on $Sr_xSm_{1-x}Fe_yC_{y-1}O_3$ perovskites synthesized at various ball milling times for use as semiconductor layers in DSSCs. Therefore, in this study, we report the synthesis of $Sr_{0.7}Sm_{0.3}Fe_{0.4}Co_{0.6}O_{2.65}$ (SSFC) perovskites by varying the ball milling time and their application as semiconductors in DSSCs.

2. Experimental section

2.1. Synthesis of SSFC

Strontium (II) acetylacetonate (97 %, Sigma-Aldrich), samarium (III) acetylacetonate hydrate (99 %, Sigma-Aldrich), iron (III) acetylacetonate (97 %, Sigma-Aldrich), and cobalt (III) acetylacetonate hydrate (97 %, Sigma-Aldrich) were used as purchased. The SSFC perovskites were prepared as reported elsewhere [13], by adding 4 g of well-mixed acetylacetonate salt (strontium (II), samarium (III), cobalt (III), and iron (III)) to a 250 ml stainless jar. Hardened stainless-steel balls of about 9 mm (ball-to-mass ratio of 12:1) were also added to the stainless jar. For SSCF-5 and SSCF-10 sample preparation, ball milling was performed using a high-energy instrument, the Retsch PM 400 MA planetary type, at 400 rpm for 5 and 10 h, respectively, under dry conditions. This was achieved by conducting ball milling for 20 min in one direction, pausing for 5 min, and reversing to another direction for 20 min during the entire 5- and 10-h periods, respectively. The ball-milled powders were calcined at 600 °C at a heating rate of 2 °C min^{-1} for 10 h using the Sentro Tech furnace. On the other hand, the SSFC-0 sample was prepared without ball milling by only mixing the powders using the mortar and pestle, followed by calcining at 600 °C.

2.2. Solar cell fabrication

The SSFC perovskite (20 mg) was added to absolute ethanol (0.10 ml) and sonicated using an ultrasonic water bath for 15 min. The dispersed mixture was deposited on the active area of an ITO glass substrate using the doctor blade method [54]. The film thickness (0.07 mm) was controlled using Scotch tape. The prepared ITO-coated glass substrate was annealed at 100 °C using a hot top plate. The prepared ITO-coated glass was loaded with eosin B dye (5, 50, and 100 mg l^{-1}). This took advantage of the high absorption of eosin B dye in the visible range (390–520 nm). The iodine-gel electrolyte was prepared as reported elsewhere [55] and added on top of the ITO-coated glass. Although gel-state electrolytes often render DSSCs with low PCEs due to their poor ionic conductivity, they significantly help to overcome flammability, leakage and evaporation issues associated with commonly used ionic liquid and organic solvent electrolytes. Device fabrication was completed by using an Al counter electrode. Despite being similar to the traditional Pt counter electrode in terms of susceptibility to corrosion, Al was employed in the present study due to its ease of availability, which renders it with a low-cost, in addition to its lightweight and competitive electrical conductivity.

2.3. Characterization

X-ray powder diffraction (XRD) of various SSFC samples was analysed using a Rigaku Miniflex600 diffractometer in the 2θ scan range from 20 to 90° with a step size of 0.02°. The Rietveld refinement technique was used to analyze and extract structural details from the XRD patterns using the FullProf program software. The generator operated at 40 kV with a high-intensity Cu-K$_{\alpha}$ radiation source at a wavelength of 0.154 nm. Firstly, the main parameters, such as background and scale factors, were refined. After that, further refinement of width parameters, lattice parameters, preferred orientation, profile shape, asymmetry, atomic coordinates, site occupancies, and isothermal parameters were performed. The experimental data was fitted using computing parameters viz., Bragg factor (R$_B$), crystallographic factor (R$_F$), profile factor (R$_P$), and goodness of fit (χ^2) to attain the best fit using experimental diffraction data [56]. A high-resolution transmission electron microscope (HRTEM, JEOL JEM-2100) was used to analyze the microstructural characteristics of all samples at an accelerating voltage of 200 kV. A field emission scanning electron microscope (FESEM, JEOL JSM-6100) coupled with energy-dispersive X-ray (EDX) spectroscopy was used to examine the elemental composition, morphology, and size distribution of SSFC. The particle sizes of SSFC were estimated using the Image J software. Fourier transform infrared (FTIR) spectroscopy was employed to analyze the spectra of different perovskites using a PerkinElmer spectrum 100 utilizing the Universal ATR sampling accessory ranging from 450 to 4000 cm^{-1}. Raman analysis was used to study the crystallinity of SSFC using a DeltaNu Advantage 532™ Raman spectrometer. Nitrogen adsorption-desorption was used to examine the surface areas of SSFC using the Micromeritics Tristar II 3020 instrument. Thermogravimetric analysis (TGA) was done using the SDT-Q600 thermal analyzer at 25–1000 °C in air.

UV–visible (UV-Vis) absorption spectroscopy was used to examine the absorbance of SSFC using the Shimadzu UV–Vis NIR spectrophotometer. Photoluminescence (PL) spectroscopy was used to study the charge recombination rate on SSFC using the PerkinElmer LS 55 spectrofluorometer at an excitation wavelength of 310 nm. The electrical conductivity of SSFC was determined using a four-point collinear probe current-voltage (I–V) instrument and a source meter (Model 2450) SMU. Electrochemical analysis was studied using electrochemical impedance spectroscopy (EIS) with a CHI E workstation and cyclic voltammetry (CV) with a Metrohm 797 VA Compitrance electrochemical workstation. EIS and CV measurements were performed using the same three-electrode system. The reference electrode was Ag/AgCl, and the counter electrode was Pt. Firstly, 20 mg of SSFC samples were added into 2 ml of ethanol and sonicated for 30 min to obtain a well-dispersed ink. The working electrode was prepared by casting SSFC powders using a Nafion binder on the glassy carbon electrode with a 3 mm diameter and drying it with a UV lamp. The electrolyte was prepared using 3 M KOH (85, Merck) and degassed under nitrogen for 5 min before analysis. Photovoltaic measurements were carried out at room temperature using an Oriel Instruments LCS-100 solar simulator under light illumination (100 mW cm^{-2}, AM 1.5 G) with maximum power (750 W), Xenon short AKC lamp (150 W), voltage (116–220 V) and frequency (50–60 Hz) on an active area of 0.98 cm^2. A standard solar cell sample (high-quality silicon reference cell, Open RR-1002) was used to calibrate the solar system prior to taking the photovoltaic measurements at a working distance of 8.10 cm.

3. Results and discussion

3.1. Phase composition and structural properties

Powder XRD using the Rietveld method was used to analyze crystal structures and different phase compositions of SSFC ball-milled at 0, 5, and 10 h. The XRD patterns of SSFC ball-milled at various times (Fig. 1) showed well-defined sharp and intense peaks, demonstrating the high crystallinity of the samples. The intense peaks indicate the nucleation and full growth of the perovskite crystals at 600 °C. Among the prepared samples, SSFC-5 and SSFC-10 had intense 2θ peaks at 25, 33, 35, 40, 47, 58, 69, 79, and 90°, while SSFC-0 exhibited the same peaks except for the absence of 2θ peaks at 25 and 35°. The absence of 2θ peaks at 25 and 35° for SSFC-0 indicates the formation of more crystalline perovskites with no formation of secondary phases [57]. For SSFC-5 and SSFC-10, the formation of secondary phases, such as Sr_2FeO_{4-x} and $Sr_3Fe_2O_{6.75}$, were identified, respectively. The impurities can be created by the localized heating effect of the jar and ball collisions during milling, but it depends on time variation [58]. As the milling time increases, the complete formation of SSFC-10 phases is noted. The development of new phases as the milling time increases was also observed by Zuhailawati et al. [59]. For SSFC-0, the space group was I, while the space group of SSFC-5 and SSFC-10 was $I4/m$. All the SSFC samples formed a tetragonal structure. This was consistent with a study by Zhang et al. [47], which also demonstrated that perovskites calcined at 500–750 °C mainly form a tetragonal structure.

The Rietveld refined method via XRD analysis was used to verify the stoichiometries of SSFC, as shown in Table 1. The oxygen positions were kept as free parameters during refinement, while other atomic fractional positions were fixed. In addition, other parameters, such as scale factors, lattice constants, shape parameters, occupancies and isothermal parameters, were taken as free [60]. The C-file used for our structure was $SrCoO_3$ (COD-1551939), which was modified by adding Sm in the A-site and Fe in the B-site atoms [13].

The structural parameters (see Supplementary Fig. S1 and Fig. S2), with the side occupancy multiplied by multiplicity, were used to calculate the crystal structure stoichiometries as $Sr_{0.7}Sm_{0.3}Fe_{0.4}Co_{0.6}O_{2.65}$ (SSFC). Similar observations were obtained by Ndlovu et al. [13]. The average crystallite sizes (D) of SSFC were estimated using the Scherrer equation (Equation (1)) via the Gaussian curve fitted on the Origin software [61]:

$$D = \frac{0.9\,\lambda}{\beta\,cos\,\theta} \tag{1}$$

where λ is the X-ray wavelength (1.5406 Å, β stands for full-width at half maximum (FWHM) of the diffraction line, and θ is the Bragg

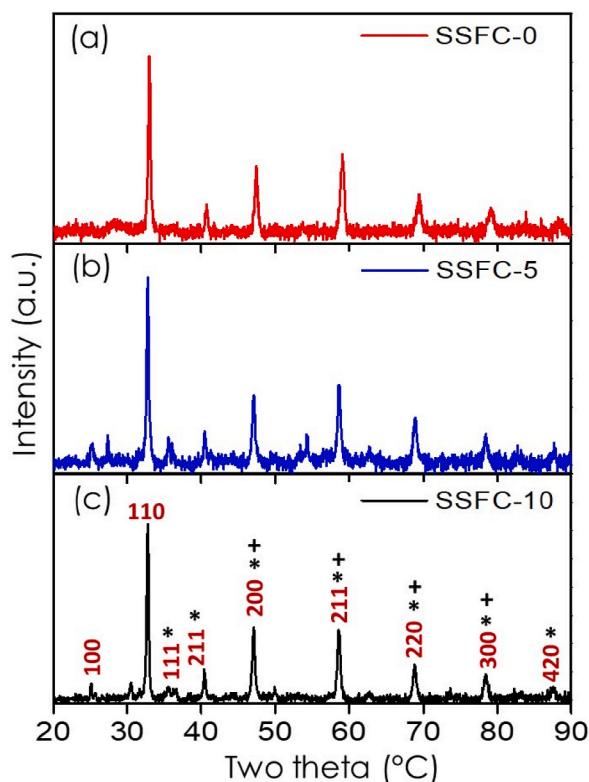**Fig. 1.** X-ray diffractograms of (a) SSFC-0, (b) SSFC-5, and (c) SSFC-10. The symbols * and+denote Sr_2FeO_{4-x} and $Sr_3Fe_2O_{6.75}$, respectively.

Table 1

The mean crystallite size, interlayer spacing, and element site occupancies for SSFC.

Milling time (h)	Mean crystallite size (nm)	Interlayer spacing (Å)	Element site occupancies				
			Sr	Sm	Fe	Co	O
0	40.9	1.952	0.702	0.298	0.399	0.601	2.652
5	23.7	2.256	0.700	0.300	0.398	0.602	2.623
10	19.7	2.263	0.704	0.296	0.400	0.600	2.650

diffraction angle. The calculated mean crystallite sizes of SSFC were 40.9, 23.7, and 19.7 nm for SSFC-0, SSFC-5, and SSFC-10, respectively. The observed decrease in mean crystallite sizes highly depends on the strong collision impact between the perovskite powder and the balls, significantly reducing crystallite sizes. Also, increased milling time allows the effective breaking of the large particles to form smaller particles due to cold welding and excessive thermal energy accumulation during milling [58]. The lattice parameters were found to be 1.952, 2.256, and 2.263 Å for SSFC-0, SSFC-5, and SSFC-10, respectively, as calculated using Equation (2) [62].

$$a = \frac{\lambda}{2} \; x \; sin\,\theta \; x \; \sqrt{h^2 + k^2 + l^2}$$

(2)

where λ represents the X-ray wavelength, θ is the (2θ value/2), and (h, k, and l) are Miller indices of the crystal lattice. Increasing the milling time to 5 and 10 h led to the creation of atomic defects, which affected the lattice [63], resulting in the observed lattice expansion. This trend was associated with the milling treatment, which leads to vacancy and grain boundary defects as the result of internal tensile strain that causes weak atomic arrangement on the structures [64]. This was comparable to Bolokang et al. [65], who also observed lattice expansion during milling. The change in lattice parameters can also be associated with oxygen nonstoichiometric vacancies [37,66].

3.2. Microstructure and morphology

3.2.1. HR-TEM analysis

The HR-TEM and selected area diffraction (SAED) images are shown in Fig. 2. The SAED patterns shown in Fig. 2(a–c) were used to study the crystalline structures of the samples. The SAED patterns revealed diffraction rings that were associated with the (100), (110), (111), (200), (211), and (420) planes, which was consistent with XRD analysis. On the other hand, the HR-TEM images shown in Fig. 2 (d–f) were used to examine the microstructure of the samples. An increase in milling time was noted to reduce the particle sizes from 40.2 nm for SSFC-0 to 23.1 and 18.9 nm for SSFC-5 and SSFC-10, respectively, due to the impact of collisions between the balls and the powder [67]. Therefore, ball milling can be used as an effective technique to reduce particle sizes, which is beneficial for increasing the
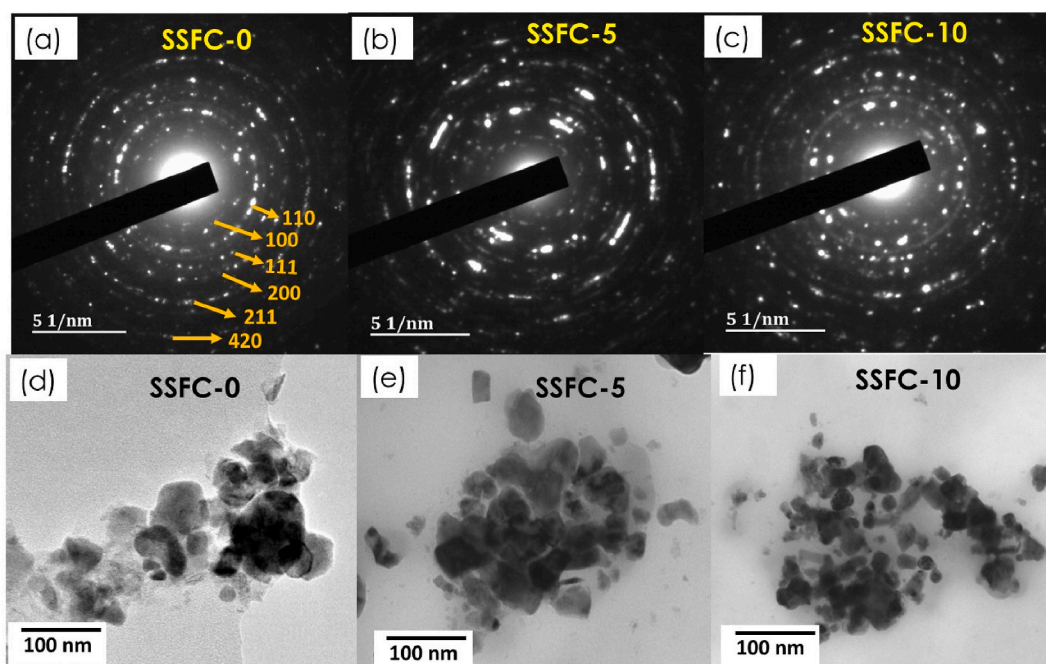
Fig. 2. SAED patterns of (a) SSFC-0, (b) SSFC-5, and (c) SSFC-10. HR-TEM images of (d) SSFC-0, (e) SSFC-5, and (f) SSFC-10.

surface area of materials.

3.2.2. FESEM analysis

The surface morphology of prepared samples was investigated using FESEM. The FESEM images in Fig. 3(a–c) showed that the particles were spherical and irregularly shaped with a uniform particle size distribution. A similar trend was observed by Janbutrach et al. [68]. Interestingly, an increase in ball milling time led to a significant reduction in nanoparticle agglomeration. This is because the kinetic energy due to colliding particles can affect the compound by exerting forces in different directions based on the accumulated thermal energy, which strongly reduces the agglomeration of particles [58]. In addition, the EDX spectrum and elemental mapping shown in Fig. 3 (d) and (e) for SSFC-10 revealed the presence of homogenously distributed Sr, Sm, Fe, Co, and O elements.

3.3. Functional groups

The different functional groups present in SSFC were confirmed using FTIR analysis, as shown on the spectra in Fig. 4. All samples showed the same strong vibrational bands at 439, 550, 853, and 1444 cm^{-1} [50]. The B-site cations (Fe and Co) on the ABO$_3$ formula
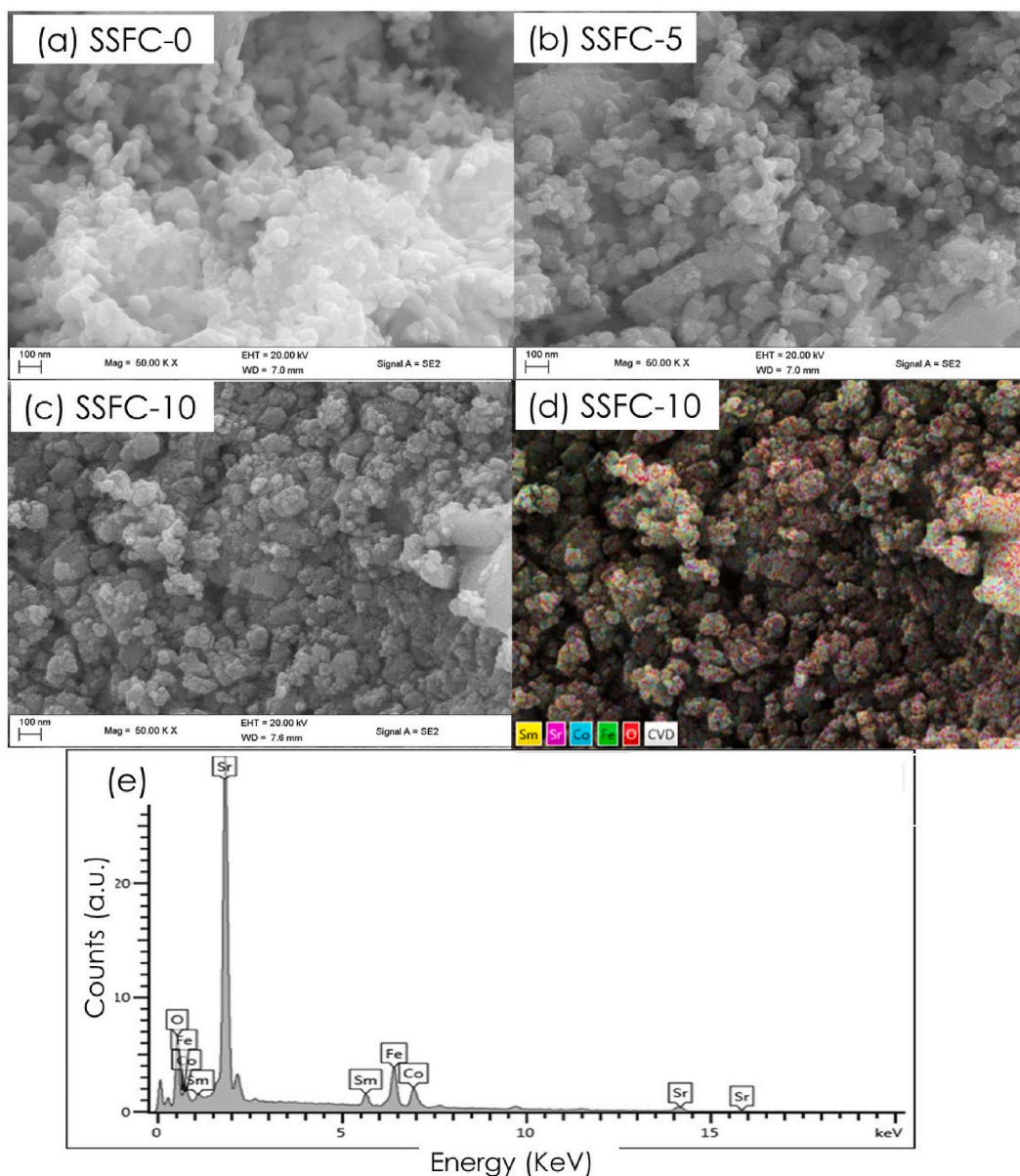

Fig. 3. FESEM images of (a) SSFC-0, (b) SSFC-5, and (c) SSFC-10. (d) SSFC-10 elemental mapping and (e) EDX spectrum.
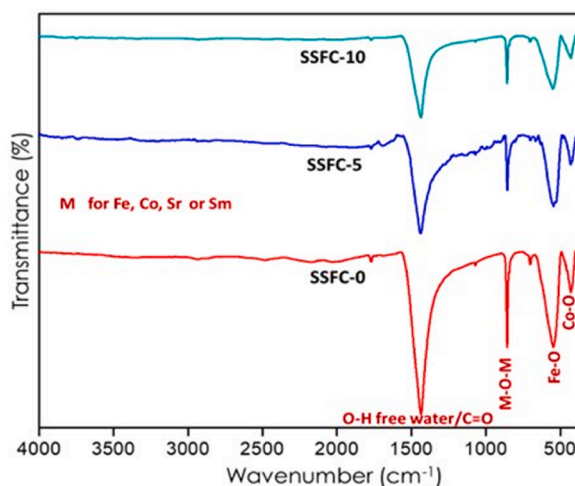
Fig. 4. FTIR spectra of SSFC-0, SSFC-5, and SSFC-10 perovskites.

occupied an octahedral environment [69]. The hematite or magnetite form of iron (Fe–O vibration) had IR bands in the 400 to 600 cm^{-1} range, depending on the annealing temperature. For instance, the 439 and 550 cm^{-1} bands represented metal-oxygen bonding, i. e., Co–O and Fe–O, respectively [35]. Moreover, the band at 853 cm^{-1} was associated with the symmetric stretching modes of the M-*O*-M (Sr/Sm–O) intermediate or resonance structure [35]. The broad peak at 1444 cm^{-1} was assigned to the stretching and bending vibration of absorbed water molecules on the surface of SSFC [37]. Thus, this peak can further indicate the carboxylic acid band formed by coupling the C–O stretching and O–H deformation vibrations [70]. Additionally, the peak at 1444 cm^{-1} was noted to decrease with an increase in milling time due to the removal of water molecules adsorbed on the perovskite samples. At around 3500 cm^{-1}, there was no water present or moisture absorbed by SSFC.

3.4. Structural properties

Raman analysis was used to examine the structural information and electronic properties of various SSFC samples, as shown in Fig. 5. All samples exhibited a tetragonal crystal structure. As predicted by the group theory, the *I*4/*m* structure has nine Raman-active modes denoted as M = $3A_g + 3B_g + 3E_g$ Ref. [71]. Much stronger bands could overlap some weak bands. Moreover, some symmetric modes were smaller than expected due to the accidental degeneracy of different modes [71], and some weak bands were observed at 300, 495, 1400, and 2455 cm^{-1}. Perovskites with strontium introduced as the A-site cation had an additional band at around 150 - 350 cm^{-1}, which reveals the formation of a low symmetry structure due to the smaller Sr ions [72]. The obtained Raman spectra did not have similar intensities, indicating that the SSFC compounds did not crystallize with the same symmetry when milling time was varied. The crystallinity of SSFC perovskites was noted to decrease with increasing milling time. This could be due to the increase in defects created on the perovskite structure that act as active sites to enhance electrochemical properties. Also, the defects on perovskite particles might affect oxygen vacancy concentration, which can result in less electron-rich oxygen species [73].
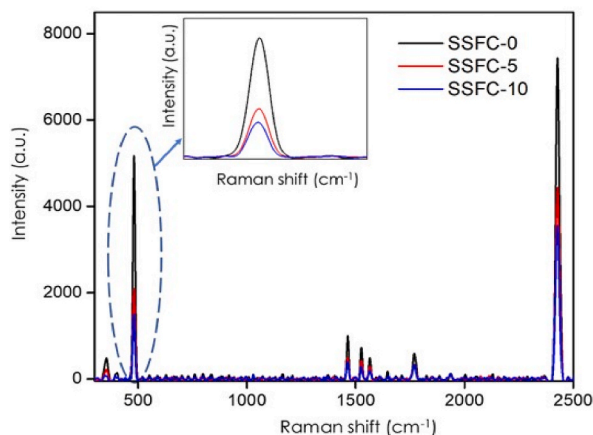

Fig. 5. Raman spectra of SSFC-0, SSFC-5, and SSFC-10 perovskites.

3.5. Surface area and porosity

The nitrogen adsorption-desorption isotherms were used to measure the surface area and porosity of SSFC perovskites using the Brunauer-Emmett-Teller (BET) technique. The BET surface areas and porosities of SSFC are shown in Table 2. The surface area values ranged between 26.2 and 61.8 $m^2\ g^{-1}$, with SSFC-10 having the highest surface area. Thus, the surface area increased with milling time, which was associated with the observed decrease in SSFC particle sizes with some defects responsible for providing more active sites.

When the balls collide with the powder in the jar for a longer time during milling, smaller nanoparticles with smaller pores will be formed. In previous studies [74,75], ball milling has produced powders with large surface areas of up to 100 $m^2\ g^{-1}$, depending on the synthesis parameters. In this study, the nitrogen adsorption-desorption isotherms (Fig. 6) were type IV with H3 hysteresis loops, as specified by the IUPAC scale [76], which reveals that the prepared materials are mesoporous. The width of the hysteresis loop became narrow with increasing milling time, which indicated an increase in surface area and a decrease in pore volume. The small particle sizes, high surface areas and small pore sizes are desirable for improving the electrochemical properties of materials.

3.6. Thermal stability

The decomposition behaviour and derivative plots of SSFC are shown in Fig. 7 (a) and (b), respectively. The heating rate was 10 °C min^{-1} in air, and the weight derivatives showed the presence of exothermic reactions in Fig. 6 (b). A calcining temperature of 600 °C was chosen because calcining at very high temperatures can lower the surface area [77]. For SSFC prepared at 0 h, only the weight loss of absorbed water was observed, as supported by FTIR in Fig. 4. There was no weight loss after 200 °C for SSFC-0, which indicates that the perovskite crystallized fully and became more thermally stable than the ball-milled perovskites. For ball-milled SSFC, the weight loss at 0–200 °C, which can be associated with the evaporation or removal of absorbed water on the perovskite surface, was also noted. In addition, the second weight loss noted at 200–300 °C could have resulted from the removal of residual organics. Moreover, the weight loss at 300–400 °C can be associated with the slight oxidation of the oxide and the release of oxygen [78]. The weight loss at 500–700 °C can also be linked to the phase transformation of secondary phases. Thus, the increase in defect sites with ball milling time (revealed earlier by XRD analysis) led to the formation of less thermally stable SSFC perovskites.

3.7. Optoelectronic transition studies

The electronic structure and energy bandgap characteristics were explored using UV–Vis spectroscopy. The UV-VIS spectra of SSFC-0, SSFC-5, and SSFC-10 shown in Fig. 8 (a) revealed strong UV absorption at 250–380 nm. There was no significant change in the absorbance band of various SSFCs. However, with the increase in milling time (5–10 h), some redshift in the absorption edge was observed, corresponding with the decrease in energy bandgap. Ball milling for a long period has also been reported to reduce the oxygen partial pressure, resulting in some small redshift in the absorption edge [79]. Tauc plots were used to determine the energy bandgap of SSFC in Fig. 8 (b). Generally, the Tauc plot can be obtained from the plot of photon energy (hv) vs (αhv)$^{1/n}$ where α denotes the absorption coefficient, and n is the intrinsic type of band transition [80]. ABO$_3$ structured perovskites have a wide bandgap of above 3.0 eV. The wide energy bandgap can be created by a large difference between the electron negativity of the B-site cation and the oxygen anion [81]. SSFC-0 and SSFC-5 had a bandgap of 3.6 eV, while SSFC-10 exhibited a bandgap of 3.1 eV. The decrease in energy bandgap from 3.6 to 3.1 eV can be related to oxygen vacancies, which allow the formation of impurities in energy levels, as supported by XRD analysis in Fig. 1. A similar observation was also made by Chen et al. [82].

3.8. Electron-hole transition studies

PL spectroscopy is a technique used to study the efficiency of charge carrier migration in materials [83,84]. Fig. 9 (a) shows the basic charge transport and transfer processes, where the orange arrows 3, 4, and 8 reveal the charge lost reactions, while the purple arrows 1, 2, 5, 6, and 7 represent electron transfer [13]. Upon illumination, the dye molecules absorb sunlight and get excited from the ground state to a higher energy state (1). The excited dye molecules are then oxidized, injecting electrons into the conduction band of SSFC (arrow 2). As illustrated by arrow 5, electrons move freely on the semiconductor since it is conductive at this energy level. This leads to the transfer of electrons to the transparent conducting electrode, where they are further transported to an external circuit to power a connected load. Consequently, as illustrated by arrow 6, an iodine electrolyte is regenerated by reducing triiodide at the counter electrode. On the other hand, upon transportation to the conduction band, a back reaction can occur, e.g., the recombination of SSFC conduction band electrons with an oxidized dye molecule (3), as well as the recombination of SSFC electrons with an iodine electrolyte (4), which lowers the efficiency of DSSCs [13]. The PL spectra of SSFC samples exhibited a broad-spectrum width (670–730
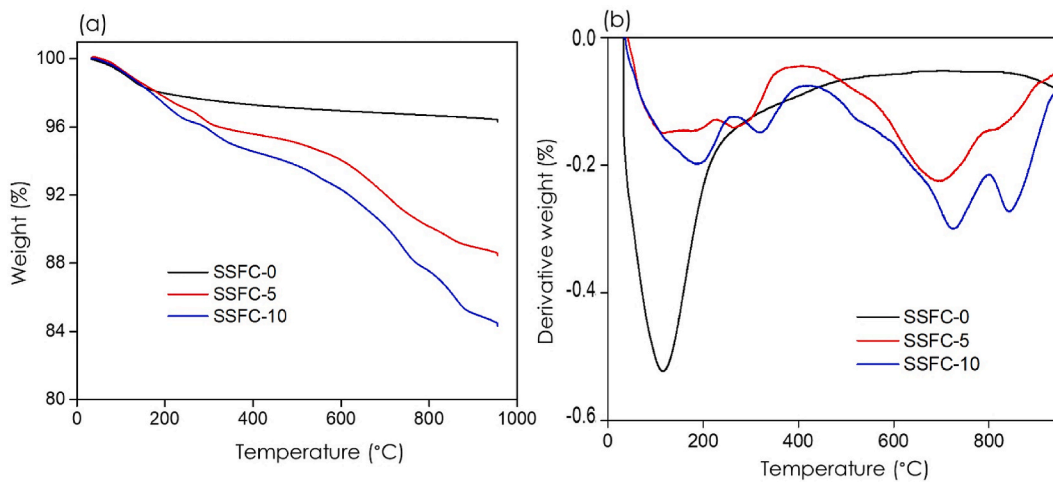
Table 2
Surface areas and porosities of SSFC-0, SSFC-5, and SSFC-10.

Milling time (h)	Surface area ($m^2\ g^{-1}$)	Pore volume ($cm^3\ g^{-1}$)	Pore size (nm)
0	26.2	0.193	2.61
5	45.5	0.222	2.02
10	61.8	0.320	1.14
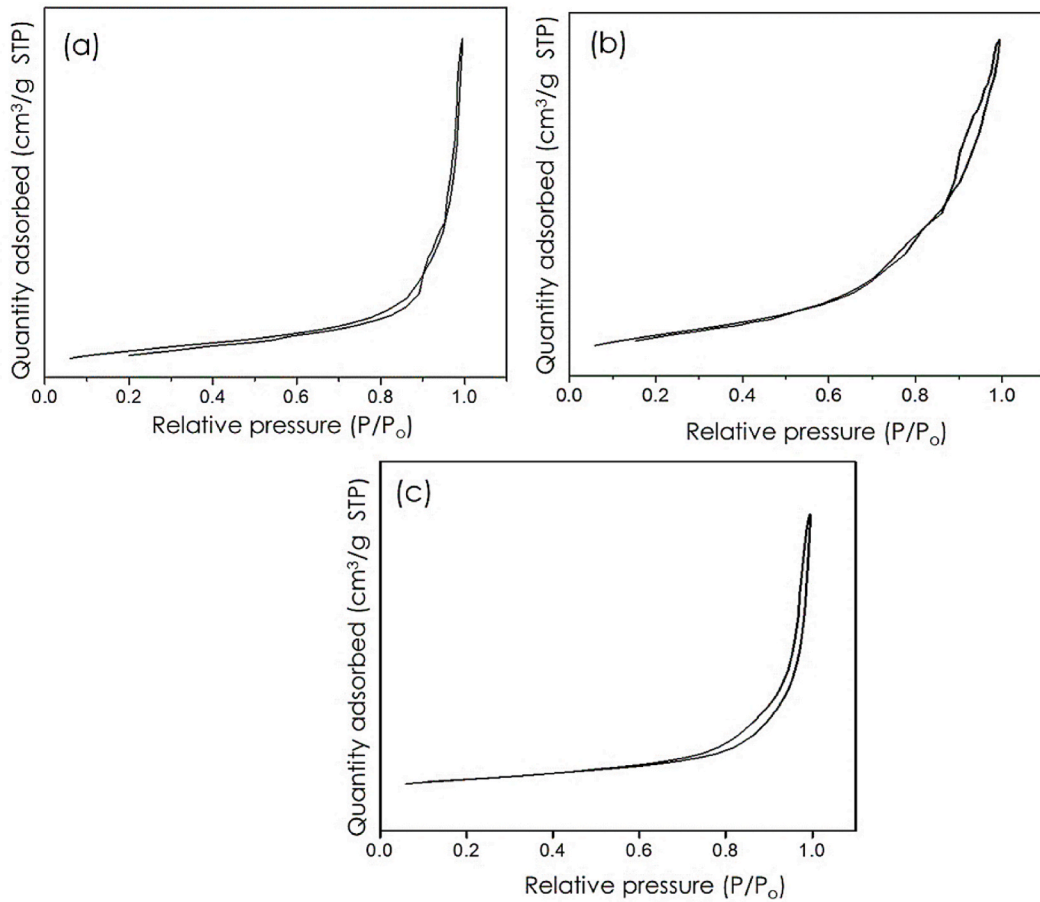
Fig. 6. Nitrogen adsorption-desorption isotherms of (a) SSFC-0, (b) SSFC-5, and (c) SSFC-10.

Fig. 7. (a) Thermograms of SSFC perovskites and (b) their first-derivative plots.

nm), which varied with the SSFC milling time, in good agreement with Yamada et al. [85]. SSFC-0 exhibited the highest intensity, which is an indication of a high charge carrier recombination rate. In contrast, SSFC-10 displayed the lowest intensity, indicating a relatively significant lower charge carrier recombination rate. The reduction in charge carrier recombination allows for the efficient transportation of photogenerated electrons in DSSCs [86]. This is related to the smaller particle sizes and high surface area, which
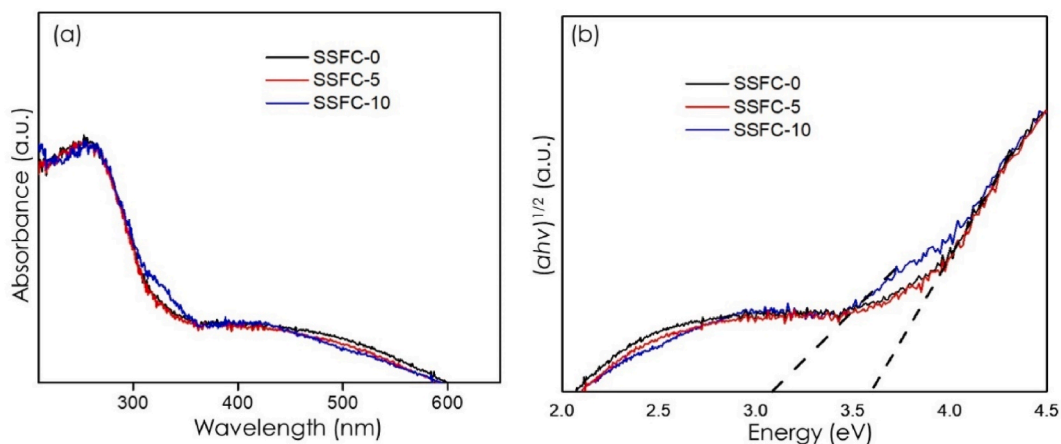
Fig. 8. (a) UV–Vis spectra and (b) energy bandgaps of prepared perovskites.
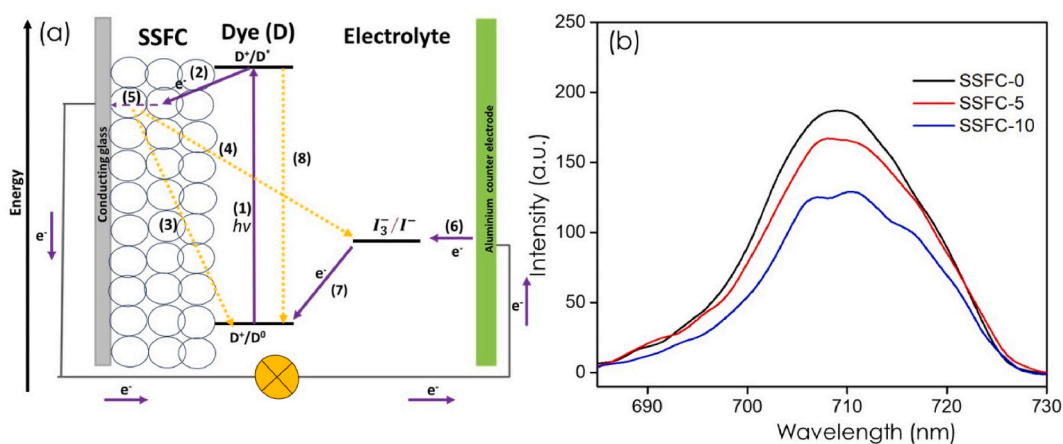

Fig. 9. (a) The basic charge transport and transfer processes. (b) PL spectra of SSFC-0, SSFC-5, and SSFC-10 perovskites.

contributed to the effective separation of photogenerated charges, thereby enhancing the efficiency of DSSCs.

3.9. Current-voltage characteristics

The electrical characterization of SSFC was conducted using a four-probe current-voltage (I–V measurement) instrument to investigate the electrical resistivity and conductivity. The resistivity (ρ) of SSFC samples was calculated using Equation (3):

$$\rho = \left(\frac{\pi}{In2}\right)\left(\frac{V}{I}\right) t \tag{3}$$

where *V*, *I*, and *t* are the voltage, current, and sheet thickness, respectively, and the obtained values are shown in Table 3. In addition, the effect of varying milling time on electrical resistivity and conductivity is shown in Fig. 10.

SSFC-0 was noted to have the lowest electrical conductivity due to the high level of absorbed water, which promotes ionic diffusivity [78]. This observation agrees with the high peak band of water presence in Figs. 4 and 7. Correspondingly, the presence of poor oxygen vacancies could have made an impact by increasing the resistivity [87]. The observed low electrical conductivity for

Table 3
Electrical resistivity and conductivity of SSFC-0, SSFC-5, and SSFC-10.

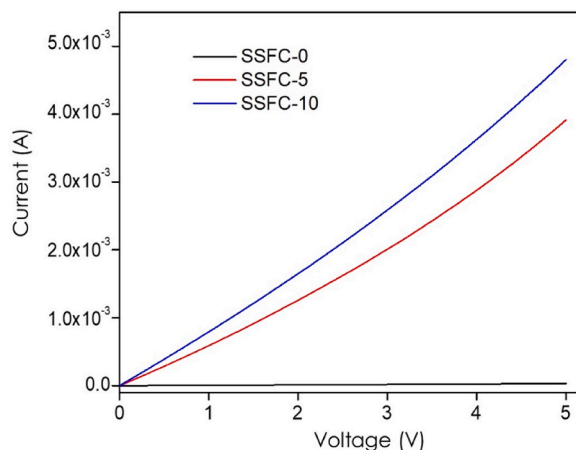| Milling time (h)	Resistivity (Ω cm)	Electrical conductivity (S cm^{-1})
0	0.0525	19.0
5	0.0265	47.7
10	0.0203	49.8

Fig. 10. I–V curve of SSFC-0, SSFC-5, and SSFC-10 perovskites.

SSFC-0 was also associated with the high charge carrier recombination rate revealed earlier by PL analysis. However, the resistivity decreased from 0.0525 to 0.0203 Ω cm with increasing ball milling time from 0 to 10 h, which, in turn, increased the conductivity from 19.0 to 49.8 S cm^{-1}. The improvement in electrical conductivities after milling could be attributed to the formation of smaller particle sizes, which rendered SSFC with a larger surface area for the efficient transfer of charge carriers. This was also ascribed to the reduction in charge carrier recombination upon milling (revealed earlier by PL analysis), which led to an increase in electrical conductivity with milling time.
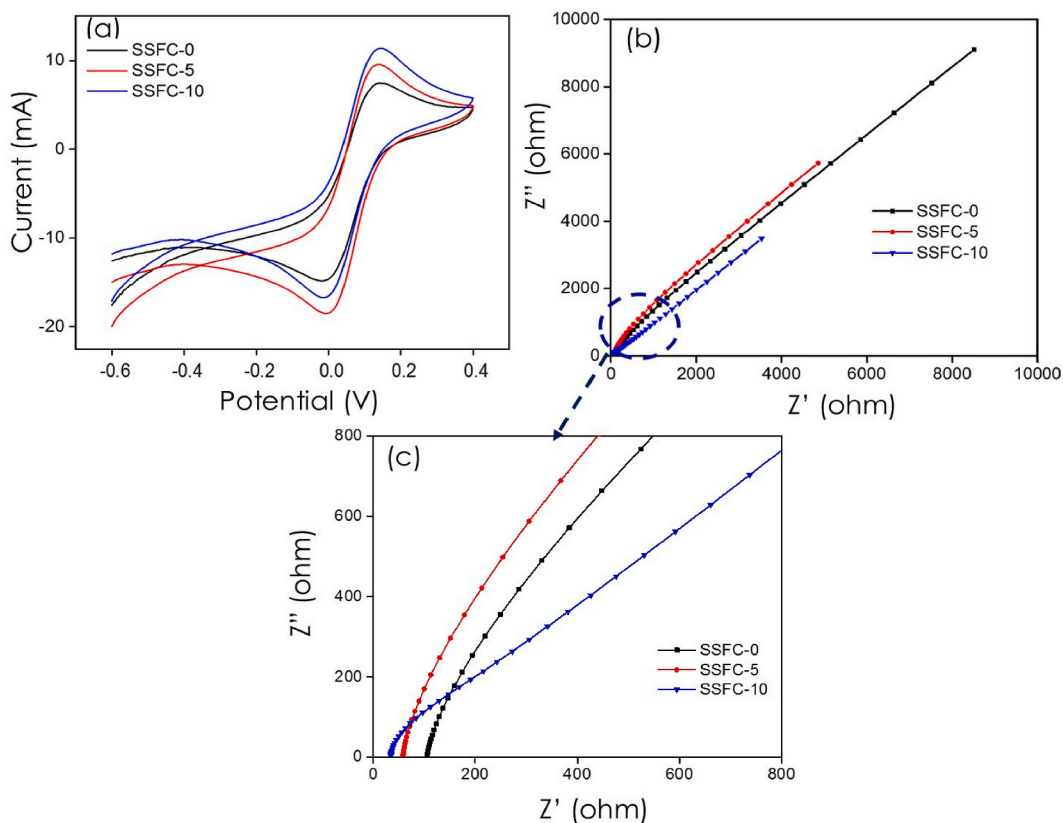

Fig. 11. (a) Cyclic voltammograms obtained at 100 mV s^{-1} for SSFC perovskites; (b) typical Nyquist plots and (c) zoom plots of SSFC perovskites.

3.10. Electrochemical properties

Cyclic voltammetry (CV) is an electrochemical technique used to study the redox potential of a reversible system [88], as shown in Fig. 11 (a). The changes in the shape of voltammograms symbolize the current change, which varies with electrode potential. The shape of voltammograms for the SSFC perovskites showed an excellent reversible Faradaic reaction after increasing the milling time. SSFC-0 displayed the smallest voltammogram shape, indicating poor charge transfer on the electrode, resulting in low electrical conductivity, as observed in Table 2. The presence of highly absorbed water on the SSFC-0 sample can increase ionic diffusivity, which ends up affecting charge transfer on the electrode. By contrast, ball-milled SSFC (5 and 10 h) displayed voltammograms with better capacitive behaviour due to enhanced surface areas. This can increase the electrolyte ion accessibility based on the active sites created by defects during milling, resulting in enhancing diffusion channels [89]. These defects on the nanoparticles can act as active sites for redox reactions while also shortening the diffusion path of ions through the electrolyte, hence causing the electrode to store more charges [78]. The improvement in capacitance upon ball milling can also be associated with the reduction in particle agglomeration observed earlier by FESEM analysis.

Complementary to CV, EIS was used to study the diffusion characteristics related to the electrochemical frequency behaviour of samples prepared at various milling times. The Nyquist plots of various SSFC perovskites are shown in Fig. 11 (b). A relatively large semicircle appeared in the Nyquist plot of the SSFC-0 electrode in the medium-high frequency region, which was attributed to the relatively high charge transfer resistance (R_{ct}) of the sample (121.5 Ω) [90,91]. On the other hand, the Nyquist plots of SSFC-5 and SSFC-10 displayed relatively small semicircles in the medium-high frequency region, indicating the presence of relatively low R_{ct}, i.e., 78.6 and 32.7 Ω, respectively. Low R_{ct} promotes effective charge transfer at the SSFC electrode/electrolyte interface, ultimately increasing the electrical conductivity and improving the DSSC performance. In addition, the relatively large slopes observed for the inclined lines in the low-frequency region upon ball milling revealed the presence of a low Warburg impedance, which is desirable for the efficient diffusion of ions within the SSFC electrode.

3.11. Photovoltaic characteristics of the fabricated DSSCs

DSSCs were fabricated using SSFC perovskites as semiconductor layers. Various photovoltaic characteristics, such as open-circuit voltage (V_{oc}), fill factor (FF), short-circuit current density (Jsc) and PCE, were obtained, and are listed in Table 4, together with the J-V curves presented in Fig. 12. The variation of dye loading concentration can strongly affect the photocurrent density of DSSCs. Three photovoltaic devices were tested for each one of the SSFC samples (0/5/10), and the best data was reported. The dye loading concentrations of 5, 50, and 100 mg l^{-1} were tested in DSSCs, as revealed in Table S1 and Fig. S3. Both 5 and 50 mg l^{-1} dye loading revealed the presence of low light absorption, low charge carrier generation, and poor charge transportation and collection in the devices. However, when 100 mg l^{-1} of eosin B dye was loaded onto the semiconductor layer, there was a significant improvement in J_{sc}, FF, and PCE mainly due to superior light absorption, which, in turn, allowed for efficient charge carrier generation and transportation. Therefore, this work focused on using the optimum dye loading concentration of 100 mg l^{-1} to obtain optimum efficiency in the devices.

The V_{oc} value can be affected by the difference between the redox potential (electrolyte) and the Fermi level of the SSFC perovskite (photoanode). The slightly low V_{oc} in SSFC-0 could be attributed to a mismatch of band structure with eosin B dye as well as poor electron transportation from excited dye to SSFC [24]. SSFC-0 exhibited low J_{sc} and FF values due to poor light absorption, resulting in less excited electrons and reduced electron injection rate into the SSFC-0 conduction band. Consequently, DSSCs with SSFC-0 semiconductor layers displayed lower PCE values than those with ball-milled SSFC (SSFC-5 and SSFC-10) semiconductor layers. Thus, the large surface areas of ball-milled samples facilitated effective dye loading, which enabled the harvesting of more incoming light for efficient charge carrier generation. This, in addition to low electrical resistivity, R_{ct} and back recombination, helped to improve the V_{oc}, FF, J_{sc}, and PCE.

Based on the J-V plots in Fig. 12, it has been noted that an increase in milling time led to a reduction in the series resistance (R_{SE}) and an increase in the shunt resistance (R_{SH}), as determined using Equations (4) and (5) [92]:

$$R_{SE} = dV/_{dJ} \quad (J = 0) \tag{4}$$

$$R_{SH} = dV/_{dJ} \ (V = 0) \tag{5}$$

The observed decrease in R_{SE} at longer milling times is desirable for suppressing resistive losses, while the increase in R_{SH} is beneficial for minimizing leakage current [14]. This, in turn, led to an increase in R_{SH}/R_{SE}, V_{oc}, J_{sc} and FF with milling time (Table 4). Therefore, the SSFC-10-based device exhibited the largest R_{SH}/R_{SE} (124.96), V_{oc} (0.71 V), J_{sc} (13.64 mA cm^{-2}), and FF (67.7 %) when compared to SSFC-0, SSFC-5 and TiO$_2$. This was consistent with a previous study by Altinkaya et al. [93]. SSFC-0-based DSSCs, on the other hand, exhibited the lowest R_{SH}/R_{SE}, V_{oc}, J_{sc} and FF when compared to their SSFC-5-, SSFC-10- and TiO$_2$-based counterparts. This could have been caused by the low electrical conductivity and high charge carrier recombination of SSFC-0, which was revealed earlier by the I–V and PL analysis. As a result, DSSCs based on SSFC-10 semiconductor layers displayed the best PCE of 6.01 %, which outperformed the PCEs of devices fabricated with an improvement of 8.67 %, 1.1 %, and 6.56 %, for SSFC-0 (3.69 %), SSFC-5 (4.96 %), and TiO$_2$ (5.64 %), respectively. This was comparable to some of the recently reported perovskite oxide-based DSSCs [50,94–101] summarized in Table 5, demonstrating that similar perovskite optimization approaches, including the nanocomposites fabrication [50, 94–99] and elemental doping [100–103], tailoring of the deposition parameters, e.g., ball milling time, also has the potential to

Table 4
Photovoltaic characteristics of various prepared SSFC perovskites.

Semiconductor	R_{SE} (Ω cm^2)	R_{SH} (Ω cm^2)	R_{SH}/R_{SE}	V_{oc} (V)	J_{sc} (mA cm^{-2})	FF (%)	PCE (%)
TiO$_2$ (ref)	8.24	352.74	42.81	0.69	11.61	62.8	5.64 ± 0.18
SSFC-0	13.16	78.96	6.00	0.61	8.81	41.3	3.69 ± 0.28
SSFC-5	11.02	124.60	11.31	0.63	10.40	59.5	4.96 ± 0.22
SSFC-10	3.89	486.10	124.96	0.71	13.64	67.7	6.01 ± 0.14
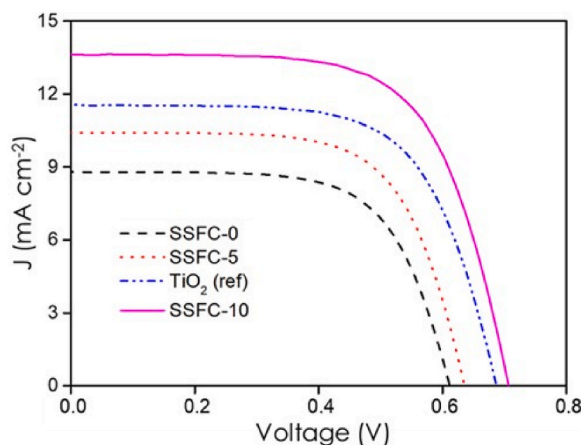
Fig. 12. The J-V characteristics of SSFC-0, SSFC-5, and SSFC-10.

Table 5
Comparison of photovoltaic parameters for recently reported DSSCs based on different perovskite oxide semiconducting layers.

Semiconducting layer	Dye	V_{oc} (V)	J_{sc} (mA cm^{-2})	FF	PCE (%)	Ref.
RGO/Sr$_{0.7}$Sm$_{0.3}$Fe$_{0.4}$Co$_{0.6}$O$_3$	Eosin B	0.84	14.02	0.77	7.25	[50]
TiO$_2$/SmFeO$_3$	N719	0.77	17.37	0.53	7.06	[94]
TiO$_2$/La$_{0.6}$Sr$_{0.4}$CoO$_3$	N719	0.75	17.32	0.46	6.04	[95]
TiO$_2$/La$_{0.6}$Sr$_{0.4}$CoO$_3$/Ag	N719	0.72	21.23	0.48	7.34	[95]
TiO$_2$/SmTiO$_3$	N719	0.74	15.07	0.47	5.31	[96]
TiO$_2$/SmTiO$_3$/Gd$_2$O$_3$	N719	0.78	18.03	0.58	8.08	[96]
TiO$_2$/AlMo$_{0.5}$O$_3$	N719	0.76	10.96	0.64	5.30	[97]
NiMnO$_3$	N3	0.81	2.13	0.35	0.60	[98]
FeMnO$_3$	N3	1.02	1.39	0.50	0.71	[98]
Ni$_{0.2}$Fe$_{0.8}$MnO$_3$	N3	0.95	1.48	0.56	0.79	[98]
BaSnO$_3$	N719	0.67	11.77	0.50	3.94	[99]
BaSnO$_3$	N719	0.60	1.62	0.67	0.65	[100]
Y–BaSnO$_3$	N719	0.80	2.08	0.71	1.17	[100]
Co–BaSnO$_3$	N719	0.84	16.85	0.58	8.22	[101]
Ag$_2$O–BiFeO$_3$	N719	0.73	0.75	0.76	4.25	[102]
Fe-doped SrLaInO$_4$	N719	0.80	11.08	0.52	4.64	[103]
Sr$_{0.7}$Sm$_{0.3}$Fe$_{0.4}$Co$_{0.6}$O$_{2.65}$	Eosin B	0.71	13.64	0.68	6.01	This study

advance DSSC performance. Thus, tuning of the deposition parameters can be employed systematically in combination with other approaches, such as chemical doping and preparation of nanocomposites, to take advantage of resulting synergistic effects further to improve the efficiency and sustainability of the device. This subsequently helps bridge the gap between DSSCs and commercially available silicon solar cells, paving the way for commercialization.

4. Conclusion

SSFC perovskites were successfully synthesized using the high-energy ball milling technique, and the effect of varying the milling time on the physicochemical properties of the prepared samples was investigated. The formation of various functional groups was noted using FTIR spectroscopy. Increasing the milling time from 0 to 10 h reduced the particle sizes, resulting in high surface areas with poor crystallinity due to the presence of high defect active sites for redox reactions, favourably improving the electrochemical properties. As a result, the SSFC-10 sample exhibited the highest surface area (61.8 m^2 g^{-1}) and best electrical conductivity (49.8 S cm^{-1}), which subsequently led to the fabrication of SSFC-10 photoanode-based DSSCs with an enhanced PCE of 6.01 % owing to the

improvement in eosin B dye loading, light absorption, charge carrier generation and charge carrier transport within the device. Therefore, varying the milling time during the synthesis can modify several properties of SSFC perovskites to allow these materials to be useful as photoanode materials in DSSCs.

Funding

CRediT authorship contribution statement

Samantha Ndlovu: Writing – review & editing, Writing – original draft, Visualization, Validation, Methodology, Investigation, Formal analysis, Data curation, Conceptualization. **Edigar Muchuweni:** Writing – review & editing, Validation, Supervision. **Vincent O. Nyamori:** Writing – review & editing, Supervision, Software, Resources, Project administration, Conceptualization.

Declaration of competing interest

The authors declare that they have no known competing financial interests or personal relationships that could have appeared to influence the work reported in this paper.

Acknowledgements

Appendix A. Supplementary data

Supplementary data to this article can be found online at https://doi.org/10.1016/j.heliyon.2024.e33347.

References

[1] M. Akhtaruzzaman, M. Shahiduzzaman, V. Selvanathan, K. Sopian, M.I. Hossain, N. Amin, A.M. Hasan, Enhancing spectral response towards high-performance dye-sensitised solar cells by multiple dye approach: a comprehensive review, Appl. Mater. Today 25 (2021) 101204, https://doi.org/10.1016/j.apmt.2021.101204.

[2] P.S. Saud, A. Bist, A.A. Kim, A. Yousef, A. Abutaleb, M. Park, S.-J. Park, B. Pant, Dye-sensitized solar cells: fundamentals, recent progress, and optoelectrical properties improvement strategies, Opt. Mater. 150 (2024) 115242, https://doi.org/10.1016/j.optmat.2024.115242.

[3] R. Kaur, N. Dalpati, J.H. Delcamp, B.H. Farnum, Nickel-based two-electron redox shuttle for dye-sensitized solar cells in low light applications, ACS Appl. Energy Mater. 7 (2024) 3645, https://doi.org/10.1021/acsaem.3c03198.

[4] H.K. Kim Masud, Redox shuttle-based electrolytes for dye-sensitized solar cells: comprehensive guidance, recent progress, and future perspective, ACS Omega 8 (2023) 6139, https://doi.org/10.1021/acsomega.2c06843.

[5] Launch of New RICOH EH DSSC Modules with 20% Increase in Power Generation | Global | Ricoh. (accessed May-5-2024).

[6] M.S. Ahmad, A.K. Pandey, N. Abd Rahim, Advancements in the development of TiO$_2$ photoanodes and its fabrication methods for dye sensitized solar cell (DSSC) applications. A review, Renew. Sustain. Energy Rev. 77 (2017) 89, https://doi.org/10.1016/j.rser.2017.03.129.

[7] H. Iftikhar, G.G. Sonai, S.G. Hashmi, A.F. Nogueira, P.D. Lund, Progress on electrolytes development in dye-sensitized solar cells, Materials 12 (2019) 1998, https://doi.org/10.3390/ma12121998.

[8] S. Ding, C. Yang, J. Yuan, H. Li, X. Yuan, M. Li, An overview of the preparation and application of counter electrodes for DSSCs, RSC Adv. 13 (2023) 12309, https://doi.org/10.1039/D3RA00926B.

[9] N. Tomar, A. Agrawal, V.S. Dhaka, P.K. Surolia, Ruthenium complexes based dye sensitized solar cells: fundamentals and research trends, Sol. Energy 207 (2020) 59, https://doi.org/10.1016/j.solener.2020.06.060.

[10] R.N. Iman, K. Harrabi, M. Younas, A. Mekki, Fabrication of efficient natural dye-sensitized solar cells using Mediterranean olive leaves as natural dye sensitizer, J. Photochem. Photobiol., A: Chem 450 (2024) 115477, https://doi.org/10.1016/j.jphotochem.2024.115477.

[11] Y. Kocak, A. Atli, A. Atilgan, A. Yildiz, Extraction method dependent performance of bio-based dye-sensitized solar cells (DSSCs), Mater. Res. Express 6 (2019) 095512, https://doi.org/10.1088/2053-1591/ab2ef7.

[12] S. Thomas, T. Deepak, G. Anjusree, T. Arun, S.V. Nair, A.S. Nair, A review on counter electrode materials in dye-sensitized solar cells, J. Mater. Chem. A 2 (2014) 4474, https://doi.org/10.1039/C3TA13374E.

[13] S. Ndlovu, E. Muchuweni, M.A. Ollengo, V.O. Nyamori, Highly efficient nitrogen-doped reduced graphene oxide-Sr$_{0.7}$Sm$_{0.3}$Fe$_{0.4}$Co$_{0.6}$O$_{2.65}$ nanocomposites utilized as a counter electrode in dye-sensitized solar cells, Mater. Today Commun. 38 (2023) 107681, https://doi.org/10.1016/j.mtcomm.2023.107681.

[14] Z. Tang, J. Wu, M. Zheng, J. Huo, Z. Lan, A microporous platinum counter electrode used in dye-sensitized solar cells, Nano Energy 2 (2013) 622, https://doi.org/10.1016/j.nanoen.2013.07.014.

[15] E.T. Mombeshora, R. Simoyi, V.O. Nyamori, P.G. Ndungu, Multiwalled carbon nanotube-titania nanocomposites: understanding nano-structural parameters and functionality in dye-sensitized solar cells, S. Afr. J. Chem. 68 (2015) 153, https://doi.org/10.17159/0379-4350/2015/v68a22.

[16] A. Yildiz, T. Chouki, A. Atli, M. Harb, S.W. Verbruggen, R. Ninakanti, S. Emin, Efficient iron phosphide catalyst as a counter electrode in dye-sensitized solar cells, ACS Appl. Energy Mater. 4 (2021) 10618, https://doi.org/10.1021/acsaem.1c01628.

[17] S. He, Z. Lan, B. Zhang, Y. Gao, L. Shang, G. Yue, S. Chen, Z. Shen, F. Tan, J. Wu, Holistically optimizing charge carrier dynamics enables high-performance dye-sensitized solar cells and photodetectors, ACS Appl. Mater. Interfaces 14 (2022) 43576, https://doi.org/10.1021/acsami.2c13009.

[18] S. He, L. Shang, Y. Gao, Y. Shi, F. Tan, X. Chen, G. Yue, Holistically modulating charge recombination via trisiloxane surface treatment for efficient dye-sensitized solar cells, J. Alloys Compd. 896 (2022) 162864, https://doi.org/10.1016/j.jallcom.2021.162864.

[19] D. Joshy, S. Narendranath, Y.A. Ismail, P. Periyat, Recent progress in one dimensional TiO$_2$ nanomaterials as photoanode in dye-sensitized solar cells, Nanoscale Adv. 4 (2022) 5202, https://doi.org/10.1039/D2NA00437B.

[20] S. Hore, E. Palomares, H. Smit, N.J. Bakker, P. Comte, P. Liska, K.R. Thampi, J.M. Kroon, A. Hinsch, J.R. Durrant, Acid versus base peptization of mesoporous nanocrystalline TiO$_2$ films: functional studies in dye sensitized solar cells, J. Mater. Chem. 15 (2005) 412, https://doi.org/10.1039/B407963A.

[21] Q. Liu, Q. Sun, M. Zhang, Y. Li, M. Zhao, L. Dong, Enhanced photoelectrical performance of dye-sensitized solar cells with double-layer TiO$_2$ on perovskite SrTiO$_3$ substrate, Appl. Phys. A 122 (2016) 1, https://doi.org/10.1007/s00339-016-9950-9.

[22] K. Salimi, A. Atilgan, M.Y. Aydin, H. Yildirim, N. Celebi, A. Yildiz, Plasmonic mesoporous core-shell Ag-Au@ TiO2 photoanodes for efficient light harvesting in dye sensitized solar cells, Sol. Energy 193 (2019) 820, https://doi.org/10.1016/j.solener.2019.10.039.

[23] A. Atilgan, A. Yildiz, Ni-doped TiO$_2$/TiO$_2$ homojunction photoanodes for efficient dye-sensitized solar cells, Int. J. Energy Res. 46 (2022) 14558, https://doi.org/10.1002/er.8175.

[24] M.S. Sheikh, A. Roy, S. Bhandari, T.K. Mallick, S. Sundaram, T. Sinha, Highly conductive double perovskite oxides A$_2$LuTaO$_6$ (A= Ba, Sr, Ca) as promising photoanode material for dye sensitized solar cells, Mater. Lett. 276 (2020) 128220, https://doi.org/10.1016/j.matlet.2020.128220.

[25] A. Roy, P.P. Das, P. Selvaraj, S. Sundaram, P.S. Devi, engineering. Perforated BaSnO$_3$ nanorods exhibiting enhanced efficiency in dye sensitized solar cells, ACS Sustain. Chem. Eng. 6 (2018) 3299, https://doi.org/10.1021/acssuschemeng.7b03479.

[26] Y. Jing, N. Aluru, The role of A-site ion on proton diffusion in perovskite oxides (ABO$_3$), J. Power Sources 445 (2020) 227327, https://doi.org/10.1016/j.jpowsour.2019.227327.

[27] N.F. Atta, A. Galal, A.R. El-Gohary, Gold-doped nano-perovskite-decorated carbon nanotubes for electrochemical sensing of hazardous hydrazine with application in wastewater sample, Sens. Actuators B Chem. 327 (2020) 128879, https://doi.org/10.1016/j.snb.2020.128879.

[28] N.F. Atta, A. Galal, S.M. Ali, The catalytic activity of ruthenates ARuO$_3$ (A= Ca, Sr or Ba) for the hydrogen evolution reaction in acidic medium, Int. J. Electrochem. Sci. 7 (2012) 725, https://doi.org/10.1016/S1452-3981(23)13372-4.

[29] H. Ekram, A. Galal, N.F. Atta, The effect of A-site doping in a strontium palladium perovskite and its applications for non-enzymatic glucose sensing, RSC Adv. 6 (2016) 16183, https://doi.org/10.1039/C5RA24107C.

[30] N.F. Atta, S.M. Ali, H. Ekram, A. Galal, Nano-perovskite carbon paste composite electrode for the simultaneous determination of dopamine, ascorbic acid and uric acid, Electrochim. Acta 128 (2014) 16, https://doi.org/10.1016/j.electacta.2013.09.101.

[31] M.K. Rath, K.-T. Lee, Superior electrochemical performance of non-precious Co-Ni-Mo alloy catalyst-impregnated Sr$_2$FeMoO$_{6-\delta}$ as an electrode material for symmetric solid oxide fuel cells, Electrochim. Acta 212 (2016) 678, https://doi.org/10.1016/j.electacta.2016.07.037.

[32] H. Corrêa, I. Cavalcante, D. Souza, E. Santos, M.D. Orlando, H. Belich, F. Silva, E. Medeiro, J. Pires, J. Passamai, Synthesis and structural characterization of the Ca$_2$MnReO$_6$ double perovskite, Cerâmica 56 (2010) 193, https://doi.org/10.1590/S0366-69132010000200015.

[33] D.S. Khaerudini, S. Alva, Nano-manipulation of Bi$_{0.7}$Sr$_{1.3}$Co$_{0.5}$Fe$_{1.5}$O$_{6-\delta}$ double perovskite oxide for oxygen separation: assessment on morphology structure and oxygen desorption properties, Adv. Nat. Sci. Nanosci. Nanotechnol. 11 (2020) 015013, https://doi.org/10.1088/2043-6254/ab798e.

[34] R. Pinedo, I.R. de Larramendi, D.J. de Aberasturi, I.G. de Muro, A.T. Aguayo, J.I.R. de Larramendi, T. Rojo, A straightforward synthesis of carbon nanotube–perovskite composites for solid oxide fuel cells, J. Mater. Chem. 21 (2011) 10273, https://doi.org/10.1039/C1JM11632K.

[35] M.N. Sithole, B. Omondi, P.G. Ndungu, Synthesis and characterization of Ce$_{0.6}$Sr$_{0.4}$Fe$_{0.8}$Co$_{0.2}$O$_{3-\delta}$ perovskite material: potential cathode material for low temperature SOFCs, J. Rare Earths 35 (2017) 389, https://doi.org/10.1016/S1002-0721(17)60924-4.

[36] M.A. Khan, K. Khan, A. Mahmood, G. Murtaza, M.N. Akhtar, I. Ali, M. Shahid, I. Shakir, M.F. Warsi, Nanocrystalline La$_{1-x}$Sr$_x$Co$_{1-y}$Fe$_y$O$_3$ perovskites fabricated by the micro-emulsion route for high frequency response devices fabrications, Ceram. Int. 40 (2014) 13211, https://doi.org/10.1016/j.ceramint.2014.05.027.

[37] C.B. Njoku, R.J. Kriek, Application of Sm$_{0.8}$Sr$_{0.2}$Fe$_{1-x}$Co$_x$O$_{3-\delta}$ (x= 0.2, 0.5, 0.8) perovskite for the oxygen evolution reaction in alkaline media, Electrocatalysis 10 (2019) 305, https://doi.org/10.1007/s12678-018-0498-7.

[38] F. Aftab, S. Tanveer, S.U. Rehman, S. Ghafoor, H. Duran, K. Kirchhoff, I. Lieberwirth, S.N. Arshad, Encapsulation of Fe/Fe$_3$O$_4$ in carbon nanotubes grown over carbon nanofibers for high performance supercapacitor electrodes, Synth. Met. 269 (2020) 116575, https://doi.org/10.1016/j.synthmet.2020.116575.

[39] L. Yu, N. Xu, T. Zhu, Z. Xu, M. Sun, D. Geng, La$_{0.4}$Sr$_{0.6}$Co$_{0.7}$Fe$_{0.2}$Nb$_{0.1}$O$_{3-\delta}$ perovskite prepared by the sol-gel method with superior performance as a bifunctional oxygen electrocatalyst, Int. J. Hydrog. Energy. 45 (2020) 30583, https://doi.org/10.1016/j.ijhydene.2020.08.105.

[40] P. Mehdizadeh, O. Amiri, S. Rashki, M. Salavati-Niasari, M. Salimian, L.K. Foong, Effective removal of organic pollution by using sonochemical prepared LaFeO$_3$ perovskite under visible light, Ultrason. Sonochem. 61 (2020) 104848, https://doi.org/10.1016/j.ultsonch.2019.104848.

[41] J. Sun, Z. Zhao, Y. Li, X. Yu, L. Zhao, J. Li, Y. Wei, J. Liu, Synthesis and catalytic performance of macroporous La$_{1-x}$Ce$_x$CoO$_3$ perovskite oxide catalysts with high oxygen mobility for catalytic combustion of soot, J. Rare Earths 38 (2020) 584, https://doi.org/10.1016/j.jre.2019.05.014.

[42] K. Ogunniran, G. Murugadoss, R. Thangamuthu, P. Periasamy, Evaluation of nanostructured Nd$_{0.7}$Co$_{0.3}$FeO$_3$ perovskite obtained via hydrothermal method as anode material in Li-ion battery, Mater. Chem. Phys. 248 (2020) 122944, https://doi.org/10.1016/j.matchemphys.2020.122944.

[43] T.A. Nguyen, V. Pham, T.L. Pham, L.T.T. Nguyen, I.Y. Mittova, V. Mittova, L.N. Vo, B.T.T. Nguyen, V.X. Bui, E. Viryutina, Simple synthesis of NdFeO$_3$ nanoparticles by the co-precipitation method based on a study of thermal behaviors of Fe(III) and Nd (III) hydroxides, Crystals 10 (2020) 219, https://doi.org/10.3390/cryst10030219.

[44] L. Lin, K. Wang, R. Azmi, J. Wang, A. Sarkar, M. Botros, S. Najib, Y. Cui, D. Stenzel, P.A. Sukkurji, Mechanochemical synthesis: route to novel rock-salt-structured high-entropy oxides and oxyfluorides, J. Mater. Sci. 55 (2020) 1, https://doi.org/10.1007/s10853-020-05183-4.

[45] G. Wang, J. Xu, M. Wen, R. Cai, R. Ran, Z. Shao, Influence of high-energy ball milling of precursor on the morphology and electrochemical performance of Li$_4$Ti$_5$O$_{12}$–ball-milling, Solid State Ion 179 (2008) 946, https://doi.org/10.1016/j.ssi.2008.03.032.

[46] D. Gao, J. Zhao, W. Zhou, R. Ran, Z. Shao, Influence of high-energy ball milling of the starting powder on the sintering; microstructure and oxygen permeability of Ba$_{0.5}$Sr$_{0.5}$Co$_{0.5}$Fe$_{0.5}$O$_{3-\delta}$ membranes, J. Membr. Sci. 366 (2011) 203, https://doi.org/10.1016/j.memsci.2010.10.001.

[47] L. Zhang, Z. Xu, L. Cao, X. Yao, Synthesis of BF–PT perovskite powders by high-energy ball milling, Mater. Lett. 61 (2007) 1130, https://doi.org/10.1016/j.matlet.2006.06.069.

[48] E. Campagnoli, A. Tavares, L. Fabbrini, I. Rossetti, Y.A. Dubitsky, A. Zaopo, L. Forni, Effect of preparation method on activity and stability of LaMnO$_3$ and LaCoO$_3$ catalysts for the flameless combustion of methane, Appl. Catal., B 55 (2005) 133, https://doi.org/10.1016/j.joule.2020.06.004.

[49] J. Park, J. Zou, H. Yoon, G. Kim, J.S. Chung, Electrochemical behavior of Ba$_{0.5}$Sr$_{0.5}$Co$_{0.2-x}$Zn$_x$Fe$_{0.8}$O$_{3-\delta}$ (x= 0–0.2) perovskite oxides for the cathode of solid oxide fuel cells, Int. J. Hydrog. Energy. 36 (2011) 6184, https://doi.org/10.1016/j.ijhydene.2011.01.142.

[50] S. Ndlovu, E. Muchuweni, M.A. Ollengo, V.O. Nyamori, Tuning the properties of reduced graphene oxide-Sr$_{0.7}$Sm$_{0.3}$Fe$_{0.4}$Co$_{0.6}$O$_3$ nanocomposites as potential photoanodes for dye-sensitized solar cells, J. Electron. Mater. 52 (2023) 5843, https://doi.org/10.1007/s11664-023-10526-3.

[51] A. Alizadeh, M. Roudgar-Amoli, Z. Shariatinia, E. Abedini, S. Asghar, S. Imani, Recent developments of perovskites oxides and spinel materials as platinum-free counter electrodes for dye-sensitized solar cells: a comprehensive review, Renew. Sustain. Energy Rev. 187 (2023) 113770, https://doi.org/10.1016/j.rser.2023.113770.

[52] M. García-Rodríguez, J.X. Flores-Lasluisa, D. Cazorla-Amorós, E. Morallón, Metal oxide perovskite-carbon composites as electrocatalysts for zinc-air batteries. Optimization of ball-milling mixing parameters, J. Colloid Interface Sci. 630 (2023) 269, https://doi.org/10.1016/j.jcis.2022.10.086.

[53] M. Fabián, B.I. Arias-Serrano, J. Briančin, A. Yaremchenko, Mechanosynthesis and electrical conductivity of undoped and calcium-substituted GdAlO$_3$ perovskites, J. Alloys Compd. 965 (2023) 171374, https://doi.org/10.1016/j.jallcom.2023.171374.

[54] I.-K. Ding, J. Melas-Kyriazi, N.-L. Cevey-Ha, K.G. Chittibabu, S.M. Zakeeruddin, M. Grätzel, M.D. McGehee, Deposition of hole-transport materials in solid-state dye-sensitized solar cells by doctor-blading, Org. Electron. 11 (2010) 1217, https://doi.org/10.1016/j.orgel.2010.04.019.

[55] H. Gerischer, Charge transfer processes at semiconductor-electrolyte interfaces in connection with problems of catalysis, Surf. Sci. 18 (1969) 97, https://doi.org/10.1016/0039-6028(69)90269-6.

[56] S. Carbonin, F. Martignago, G. Menegazzo, A. Dal Negro, X-ray single-crystal study of spinels: in situ heating, Phys. Chem. Miner. 29 (2002) 503, https://doi.org/10.1007/s00269-002-0262-6.

[57] I. Abdulkadir, S.B. Jonnalagadda, B.S. Martincigh, Synthesis and effect of annealing temperature on the structural, magnetic and photocatalytic properties of $(La_{0.5}Bi_{0.2}Ba_{0.2}Mn_{0.1})FeO_{(3-\delta)}$, Mater. Chem. Phys. 178 (2016) 196, https://doi.org/10.1016/j.matchemphys.2016.05.007.

[58] D.S. Khaerudini, S. Alva, Nano-manipulation of $Bi_{0.7}Sr_{1.3}Co_{0.5}Fe_{1.5}O_{6-\delta}$ double perovskite oxide for oxygen separation: assessment on morphology structure and oxygen desorption properties, Adv. Nat. Sci. Nanosci. Nanotechnol. 11 (2020) 015013, https://doi.org/10.1088/2043-6254/ab798e.

[59] H. Zuhailawati, Y. Mahani, Effects of milling time on hardness and electrical conductivity of in situ Cu–NbC composite produced by mechanical alloying, J. Alloys Compd. 476 (2009) 142, https://doi.org/10.1016/j.jallcom.2008.09.018.

[60] L. Kumar, P. Kumar, A. Narayan, M. Kar, Rietveld analysis of XRD patterns of different sizes of nanocrystalline cobalt ferrite, Int. Nano Lett. 3 (2013) 1, https://doi.org/10.1186/2228-5326-3-8.

[61] M. Iqbal, R. Kriek, Silver/nickel oxide (Ag/NiO) nanocomposites produced via a citrate sol-gel route as electrocatalyst for the oxygen evolution reaction (OER) in alkaline medium, Electrocatalysis 9 (2018) 279, https://doi.org/10.1007/s12678-018-0455-5.

[62] C.B. Njoku, P.G. Ndungu, Synthesis and characterization of novel $Ce0.8Sm0.2Fe0.9Ir0.03Co0.07O3-\delta$ perovskite material and possible application as a cathode for low–intermediate temperature SOFCs, Mater. Res. Bull. 68 (2015) 100, https://doi.org/10.1016/j.materresbull.2015.03.029.

[63] L. Trotochaud, S.L. Young, J.K. Ranney, S.W. Boettcher, Nickel–iron oxyhydroxide oxygen-evolution electrocatalysts: the role of intentional and incidental iron incorporation, J. Am. Chem. Soc. 136 (2014) 6744, https://doi.org/10.1021/ja502379c.

[64] J. Jiang, C. Zhang, L. Ai, Hierarchical iron nickel oxide architectures derived from metal-organic frameworks as efficient electrocatalysts for oxygen evolution reaction, Electrochim. Acta 208 (2016) 17, https://doi.org/10.1016/j.electacta.2016.05.008.

[65] A. Bolokang, M. Phasha, Solid-state transformation in ball milled nickel powder, Mater. Lett. 64 (2010) 1894, https://doi.org/10.1016/j.matlet.2010.05.052.

[66] L. Chen, P. Fleming, V. Morris, J.D. Holmes, M.A. Morris, Size-related lattice parameter changes and surface defects in ceria nanocrystals, J. Phys. Chem. C 114 (2010) 12909, https://doi.org/10.1021/jp1031465.

[67] C.I. Priyadharsini, G. Marimuthu, T. Pazhanivel, P. Anbarasan, V. Aroulmoji, S. Prabhu, R. Ramesh, Electrochemical supercapacitor studies of Ni_{2+}-doped $SrTiO_3$ nanoparticles by a ball milling method, Ionics 26 (2020) 1, https://doi.org/10.1007/s11581-019-03412-8.

[68] Y. Janbutrach, S. Hunpratub, E. Swatsitang, Ferromagnetism and optical properties of $La_{1-x}Al_xFeO_3$ nanopowders, Nanoscale Res. Lett. 9 (2014) 498, https://doi.org/10.1186/1556-276X-9-498.

[69] C.D. Chandler, C. Roger, M.J. Hampden-Smith, Chemical aspects of solution routes to perovskite-phase mixed-metal oxides from metal-organic precursors, Chem. Rev. 93 (1993) 1205, https://doi.org/10.1021/cr00019a015.

[70] Y.A. Farzin, A. Babaei, A. Ataie, Low-temperature synthesis of Sr_2FeMoO_6 double perovskite; structure, morphology, and magnetic properties, Ceram. Int. 46 (2020) 16867, https://doi.org/10.1016/j.ceramint.2020.03.264.

[71] B. Manoun, J.M. Igartua, P. Lazor, A. Ezzahi, High temperature induced phase transitions in Sr_2ZnWO_6 and Sr_2CoWO_6 double perovskite oxides: Raman spectroscopy as a tool, J. Mol. Struct. 1029 (2012) 81, https://doi.org/10.1016/j.molstruc.2012.05.077.

[72] A. Dias, L.A. Khalam, M.T. Sebastian, R.L. Moreira, Raman-spectroscopic investigation of Ba_2InTaO_6 and Sr_2InTaO_6 perovskites, J. Solid State Chem. 180 (2007) 2143, https://doi.org/10.1063/1.4980510.

[73] Y.C. Zhang, N. Afzal, L. Pan, X. Zhang, J.J. Zou, Structure-activity relationship of defective metal-based photocatalysts for water splitting: experimental and theoretical perspectives, Adv. Sci. 6 (2019) 1900053, https://doi.org/10.1002/advs.201900053.

[74] E. Campagnoli, A. Tavares, L. Fabbrini, I. Rossetti, Y.A. Dubitsky, A. Zaopo, L. Forni, Effect of preparation method on activity and stability of $LaMnO_3$ and $LaCoO_3$ catalysts for the flameless combustion of methane, Appl. Catal., B 55 (2005) 133, https://doi.org/10.1016/j.apcatb.2004.07.010.

[75] V. Szabo, M. Bassir, A. Van Neste, S. Kaliaguine, Perovskite-type oxides synthesized by reactive grinding: part II: catalytic properties of $LaCo_{(1-x)}Fe_xO_3$ in VOC oxidation, Appl. Cataly. B. 37 (2002) 175, https://doi.org/10.1016/S0926-3373(01)00328-9.

[76] K.S. Sing, Reporting physisorption data for gas/solids systems with special reference to the determination of surface area and porosity (provisional), Pure Appl. Chem. 54 (1982) 2201, https://doi.org/10.1351/pac198254112201.

[77] Y. Sun, N. Yan, J. Li, H. Wu, J.-L. Luo, K.T. Chuang, The effect of calcination temperature on the electrochemical properties of $La_{0.3}Sr_{0.7}Fe_{0.7}Cr_{0.3}O_{3-x}$ (LSFC) perovskite oxide anode of solid oxide fuel cells (SOFCs), Sustain. Energy Technol. Assess. 8 (2014) 92, https://doi.org/10.1016/j.seta.2014.08.001.

[78] J.-K. Chang, Y.-L. Chen, W.-T. Tsai, Effect of heat treatment on material characteristics and pseudo-capacitive properties of manganese oxide prepared by anodic deposition, J. Power Sources 135 (2004) 344, https://doi.org/10.1016/j.jpowsour.2004.03.076.

[79] M. Wu, X. Lou, T. Li, J. Li, S. Wang, W. Li, B. Peng, G. Gou, Ni-doped $SrBi_2Nb_2O_9$–perovskite oxides with reduced band gap and stable ferroelectricity for photovoltaic applications, J. Alloys Compd. 724 (2017) 1093, https://doi.org/10.1016/j.jallcom.2017.04.256.

[80] N.D. Quan, V.N. Hung, N.V. Quyet, H.V. Chung, D.D. Dung, Band gap modification and ferroelectric properties of $Bi_{0.5}(Na, K)_{0.5}TiO_3$-based by Li substitution, AIP Adv. 4 (2014) 017122, https://doi.org/10.1063/1.4863092.

[81] I. Grinberg, D.V. West, M. Torres, G. Gou, D.M. Stein, L. Wu, G. Chen, E.M. Gallo, A.R. Akbashev, P.K. Davies, Perovskite oxides for visible-light-absorbing ferroelectric and photovoltaic materials, Nature 503 (2013) 509, https://doi.org/10.1038/nature12622.

[82] G. Chen, W. Bai, L. Sun, J. Wu, Q. Ren, W. Xu, J. Yang, X. Meng, X. Tang, C.-G. Duan, Processing optimization and sintering time dependent magnetic and optical behaviors of Aurivillius $Bi_5Ti_3FeO_{15}$ ceramics, J. Appl. Phys. 113 (2013) 034901, https://doi.org/10.1063/1.4775800.

[83] J. Yu, L. Qi, M. Jaroniec, Hydrogen production by photocatalytic water splitting over Pt/TiO_2 nanosheets with exposed (001) facets, J. Phys. Chem. C 114 (2010) 13118, https://doi.org/10.1021/jp104488b.

[84] Y. Gao, Z. Shen, F. Tan, G. Yue, R. Liu, Z. Wang, S. Qu, Z. Wang, W. Zhang, Novel benzo [1, 2-b: 4, 5-b'] difuran-based copolymer enables efficient polymer solar cells with small energy loss and high VOC, Nano Energy 76 (2020) 104964, https://doi.org/10.1016/j.nanoen.2020.104964.

[85] Y. Yamada, Y. Kanemitsu, Photoluminescence spectra of perovskite oxide semiconductors, J. Lumin. 133 (2013) 30, https://doi.org/10.1002/adma.201304374.

[86] X. Qi, C. Song, W. Zhang, Y. Shi, Y. Gao, H. Liu, R. Chen, L. Shang, H. Tan, F. Tan, Bidirectional targeted therapy enables efficient, stable, and eco-friendly perovskite solar cells, Adv. Funct. Mater. 33 (2023) 2214714, https://doi.org/10.1002/adfm.202214714.

[87] Y. Xie, M.D. Scafetta, R.J. Sichel-Tissot, E.J. Moon, R.C. Devlin, H. Wu, A.L. Krick, S.J. May, Control of functional responses via reversible oxygen loss in $La_{1-x}Sr_xFeO_{3-\delta}$ films, Adv. Mater. 26 (2014) 1434, https://doi.org/10.1002/adma.201304374.

[88] M. Harikrishnan, A.J.C. Mary, A.C. Bose, Electrochemical performance of $ANiO_3$ (A= La, Ce) perovskite oxide material and its device performance for supercapattery application, Electrochim. Acta 362 (2020) 137095, https://doi.org/10.1016/j.electacta.2020.137095.

[89] G. Wang, X. Sun, F. Lu, Q. Yu, C. Liu, J. Lian, Controlled synthesis of $MnSn(OH)_6$/graphene nanocomposites and their electrochemical properties as capacitive materials, J. Solid State Chem. 185 (2012) 172, https://doi.org/10.1016/j.jssc.2011.11.015.

[90] Y. Gao, Z. Xiao, M. Cui, M.I. Saidaminov, F. Tan, L. Shang, W. Li, C. Qin, L. Ding, Asymmetric Π-bridge engineering enables high-permittivity benzo [1, 2-B: 4, 5-B'] difuran-conjugated polymer for efficient organic solar cells, Adv. Mater. 36 (2024) 2306373, https://doi.org/10.1002/adma.202306373.

[91] Y. Gao, M. Cui, S. Qu, H. Zhao, Z. Shen, F. Tan, Y. Dong, C. Qin, Z. Wang, W. Zhang, Efficient organic solar cells enabled by simple non-fused electron donors with low synthetic complexity, Small 18 (2022) 2104623, https://doi.org/10.1002/smll.202104623.

[92] C. Jiang, X. Sun, K. Tan, G. Lo, A. Kyaw, D. Kwong, High-bendability flexible dye-sensitized solar cell with a nanoparticle-modified ZnO-nanowire electrode, Appl. Phys. Lett. 92 (2008) 143101, https://doi.org/10.1063/1.2905271.

[93] C. Altinkaya, A. Atli, A. Atilgan, K. Salimi, A. Yildiz, Facile fabrication of low-cost low-temperature carbon-based counter electrode with an outstanding fill factor of 73% for dye-sensitized solar cells, Int. J. Energy Res. 44 (2020) 3160, https://doi.org/10.1002/er.5174.

[94] A. Alizadeh, Z. Shariatinia, Unveiling the influence of $SmFeO_3$-TiO_2 nanocomposites as high performance photoanodes of dye-sensitized solar cells, J. Mol. Liq. 348 (2022) 118070, https://doi.org/10.1016/j.molliq.2021.118070.

[95] M. Roudgar-Amoli, Z. Shariatinia, Synergistic influence of plasmonic Ag nanoparticles/$La_{0.6}Sr_{0.4}CoO_3$/TiO_2 heterostructured photoanodes boosted solar energy harvesting by dye-sensitized photovoltaics, Sol. Energy 252 (2023) 101, https://doi.org/10.1016/j.solener.2023.01.049.

[96] A. Alizadeh, Z. Shariatinia, Auspicious energy conversion performance of dye-sensitized solar cells based on Gd_2O_3-impregnated $SmTiO_3$ perovskite/TiO_2 nanocomposite photoelectrodes, Electrochim. Acta 450 (2023) 142280, https://doi.org/10.1016/j.electacta.2023.142280.

[97] F. Ziaeifar, A. Alizadeh, Z. Shariatinia, Dye sensitized solar cells fabricated based on nanocomposite photoanodes of TiO_2 and $AlMo_{0.5}O_3$ perovskite nanoparticles, Sol. Energy 218 (2021) 435, https://doi.org/10.1016/j.solener.2021.03.024.

[98] M. Rekha, R. Yadav, L. Cindrella, $Ni_{1-x}Fe_xMnO_3$ perovskite photoanodes for dye-sensitized solar cells (DSSCs), Opt. Mater. 143 (2023) 114172, https://doi.org/10.1016/j.optmat.2023.114172.

[99] H.A. Najafabadi, A.R. Fattahi, M. Asemi, M. Ghanaatshoar, Performance enhancement of dye-sensitized solar cells by plasma treatment of $BaSnO_3$ photoanode, J. Alloys Compd. 818 (2020) 152856, https://doi.org/10.1016/j.jallcom.2019.152856.

[100] M. Gokulnaath, V. Manikandan, S.M. Mariappan, S. Harish, J. Archana, M. Navaneethan, Tailoring the band edge potential in Y^{3+} doped $BaSnO_3$ photoanode in dye sensitized solar cell applications, J. Phys. Chem. Solids. 179 (2023) 111367, https://doi.org/10.1016/j.jpcs.2023.111367.

[101] N. Rajamanickam, S. Isogami, K. Ramachandran, Effect of Co doping for improved photovoltaic performance of dye-sensitized solar cells in $BaSnO_3$ nanostructures, Mater. Lett. 275 (2020) 128139, https://doi.org/10.1016/j.matlet.2020.128139.

[102] T. Ahamad, A. Aldalbahi, S.M. Alshehri, S. Alotaibi, S. Alzahly, Z.-B. Wang, P.X. Feng, Enhanced photovoltaic performance of dye-sensitized solar cells based Ag_2O doped $BiFeO_3$ heterostructures, Sol. Energy 220 (2021) 758, https://doi.org/10.1016/j.solener.2021.03.084.

[103] Y. Xie, M. Gu, M. Chen, L. Cao, S. Zhang, Y. Wang, F. Niu, H. Yan, Layered Fe-doped $SrLaInO_4$ perovskite electron transport layer for dye-sensitized solar cell with high open-circuit voltage, Mater. Lett. 349 (2023) 134809, https://doi.org/10.1016/j.matlet.2023.134809.